# Chapter 2

# X-ray Observations, Data Reduction, and Analysis Techniques

*This chapter presents an overview of the X-ray observations utilized in this thesis. These observations were obtained using the XMM-Newton space-based X-ray observatory. A description of the XMM-Newton satellite is provided, with a particular emphasis on its technical configuration, including details of the onboard instruments. Following this, the chapter outlines a step-by-step data reduction procedure used to convert raw observational data into the science-ready products, such as light curves and spectra, using the Science Analysis Software (SAS). Finally, the various analysis techniques employed to extract physical parameters and interpret the results are discussed, forming the basis for the scientific findings presented in subsequent chapters.*

## 2.1 XMM-Newton

The X-ray Multi-Mirror Mission – Newton (XMM-Newton) was launched by the European Space Agency (ESA) in December 1999, stands as a major milestone in the field of space-based astronomy. It is equipped with three advanced X-ray telescopes, which are designed for observing high-energy cosmic phenomena. In addition to these, it carries an Optical Monitor (OM) - a 30 cm ultraviolet/optical telescope, that enables simultaneous UV and optical observations, making XMM-Newton a powerful observatory for multi-wavelength studies. The spacecraft operates in a highly elliptical orbit around the Earth, completing each orbit in approximately 48 hours. With a perigee of about 27,000 km and an apogee nearing 107,000 km, this trajectory allows extended, uninterrupted observations while avoiding the Earth's radiation belts. The satellite is three-axis stabilized, and it achieves an impressive absolute pointing accuracy of 0.25 arcseconds over a 10-second duration, despite its 10 m length. This high pointing precision is essential for deep and stable X-ray exposures.

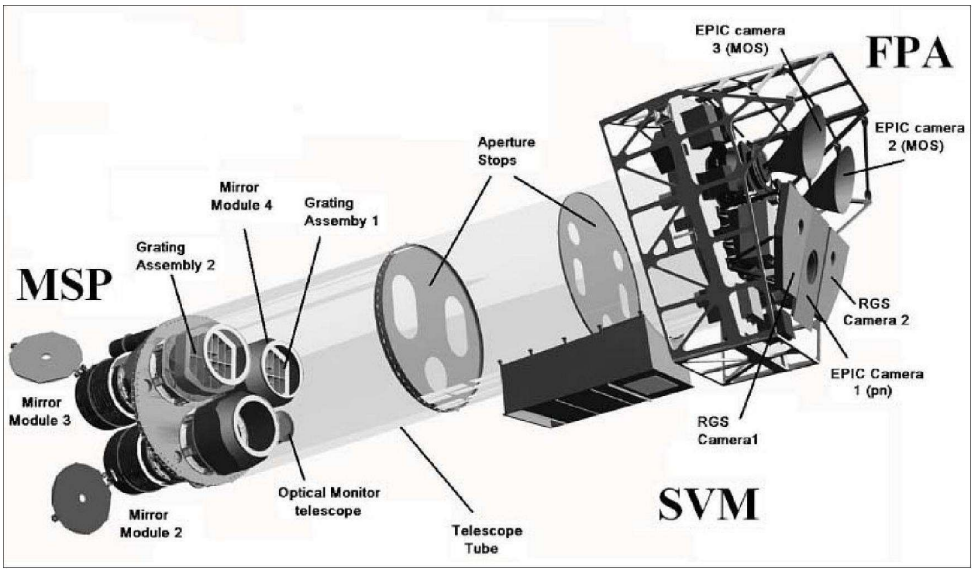


Figure 2.1: Schematic representation of an internal view of the XMM-Newton spacecraft, showing its subsystems and all the main components with outer panels removed for the better visibility. (Image credit: ESA)

Focusing X-rays is inherently challenging due to their high energy and penetrative nature. Unlike optical telescopes, the X-ray telescopes are designed in such a way as to use grazing incidence optics to reflect and focus the incoming radiations. Each of XMM-Newton's three X-ray telescopes incorporates 58 gold-coated, nested Wolter Type-I mirror shells, comprising paraboloid and hyperboloid surfaces arranged in a coaxial, confocal geometry. This design enables effective focusing of X-rays onto the detectors. Collectively, the mirror assemblies provide a combined effective area of over 120 $m^2$, offering high sensitivity across a broad X-ray energy range (Jansen et al., 2001). The optical assembly and satellite layout with all the main components marked are illustrated in Fig. 2.1.

The scientific payload comprises three primary instruments: the European Photon Imaging Camera (EPIC), the Reflection Grating Spectrometer (RGS), and the Optical Monitor (OM). In the present study, data from the EPIC and RGS instruments have been utilized, both of which are co-aligned with the telescope axis and are designed to observe X-ray emissions. These CCD-based detectors are distributed across the three X-ray telescopes in a specific configuration: one telescope directs the full X-ray flux to the EPIC-PN detector, while the other two telescopes split the incoming X-ray photons: about half are diverted to the RGS detectors (RGS1 and RGS2) via diffraction grating assemblies, and approximately 44% of the remaining flux is directed to the EPIC-MOS detectors (MOS1 and MOS2). Fig. 2.2 provides a schematic representation of this arrangement. The detailed functioning and characteristics of these detectors are discussed in the subsequent sub-sections.

### 2.1.1 European Photon Imaging Camera (EPIC)

The EPIC instrument system includes three CCD-based detectors located at the focal planes of the three mirror assemblies: two Metal-Oxide Semiconductor (MOS) detectors (Turner et al., 2001) and one PN detector (Strüder et al., 2001). The EPIC-PN detector operates

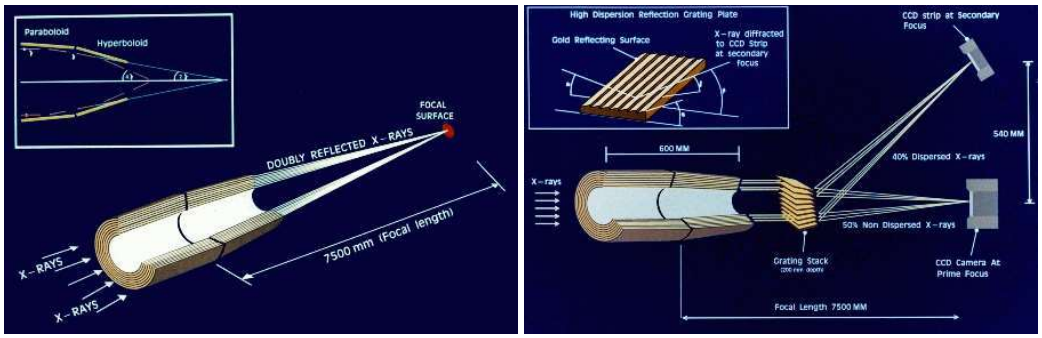


(a) (b)

Figure 2.2: (a) Schematic representation of the focusing of X-ray flux through nested Wolter Type-I mirrors, where the paraboloid and hyperboloid surfaces direct incoming X-rays onto the EPIC-PN detector. (b) Illustration of the grating assembly and the division of X-ray flux between the Reflection Grating Spectrometers and the EPIC-MOS detectors. (Image Credit: ESA)

effectively in the 0.15–15 keV energy range, while the EPIC-MOS detectors cover ~0.15 - 12 keV. Each has a field of view of 30 arcminutes and offers moderate spectral resolution ($E/\Delta E \simeq 20$–$50$). The MOS cameras consist of seven CCDs, where the outer ring of six CCDs always operates in standard Full Frame imaging mode as shown in Fig. 2.3. The central CCD, however, can be operated independently in different modes to adjust for target brightness and timing requirements. This allows simultaneous data acquisition across all CCDs, regardless of the selected mode. Whereas, the PN camera, composed of 12 CCDs integrated on a single silicon wafer as shown in Fig. 2.3, can be operated in common readout modes across all quadrants or selectively using only the central CCD (CCD 4), depending on the scientific objective.

EPIC employs Optical Blocking Filters (OBFs) to minimize contamination from optical and UV light. These filters: thick, medium, and thin are selected based on the optical brightness of the target. The thick filter offers maximum suppression, which is suitable for targets with visual magnitudes between 1 - 4 (MOS) or -2 to 1 (PN), at the cost of reduced soft X-ray sensitivity. The medium filter, approximately 100 - 1000 times less suppressive,

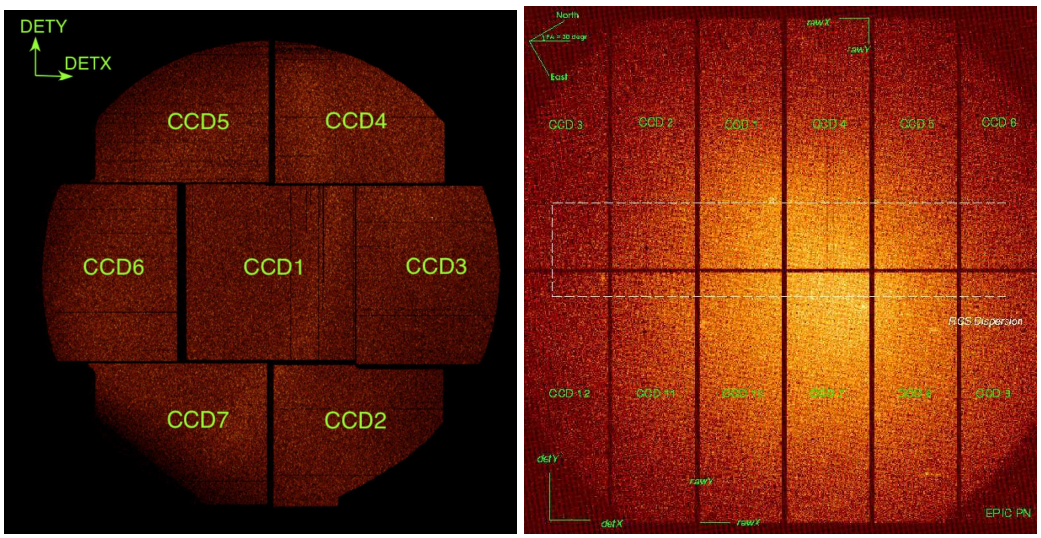


Figure 2.3: CCD chip assembly in (a) MOS detector and (B) PN detector. (Image Credit: ESA)

is used for sources in the 6–9 magnitude range. The thin filter allows maximum soft X-ray transmission and is ideal for faint targets (V > 12 mag).

EPIC detectors also support several observational modes tailored for diverse science goals. The full frame mode exposes the entire CCD array, suitable for the imaging extended sources like clusters. The large window and small window modes read out only some part of the CCD to enable faster timing resolution, with the small window being optimal for the bright, point-like sources due to even quicker readouts. The timing mode, which reads data in a one-dimensional format at very high speed, is designed for observing rapid variability in the bright sources. These modes provide flexibility in capturing both spatial and temporal information effectively.

### 2.1.2 Reflection Grating Spectrometer (RGS)

The RGS is a high-resolution dispersive spectrometer composed of two identical units placed behind two of the XMM-Newton telescopes (den Herder et al., 2001). Each unit contains an array of 182 reflection grating plates, fabricated from the silicon carbide (SiC)

and coated with a 2000 Å gold layer. These plates feature approximately 645 grooves per millimeter, enabling diffraction of the incident X-rays based on their wavelength. Incoming X-rays are thus spread into spectra, which are then focused onto dedicated RGS cameras.

Each RGS camera comprises of nine back-illuminated MOS CCDs arranged along the dispersion direction. These detectors operate in the single-photon counting and frame-transfer modes, allowing precise determination of photon positions and energies. The combination of positional and energy information helps distinguish between overlapping spectral orders. The cameras are maintained at low temperatures (~-80°C to -120°C) using passive radiators, which significantly reduces the thermal background and improves signal-to-noise ratio.

The design of the XMM-Newton optics ensures that zero-order photons are directed toward the EPIC-MOS detectors for imaging and moderate-resolution spectroscopy, while the higher-order diffracted photons are captured by the RGS for high-resolution spectral analysis. Due to the internal division of the X-ray beam, roughly 44% of the incoming photons reach the EPIC-MOS, about 40% reach the RGS, and the rest are lost.

Together, the EPIC and RGS instruments enable comprehensive investigations of X-ray sources, from broadband imaging and timing studies to the high-resolution spectral diagnostics, which makes XMM-Newton one of the most versatile and powerful observatories in X-ray astronomy to date. Focusing on two magnetically active Sun-like stars: the rapidly rotating AB Doradus and the RS CVn-type binary HR 1099, this work makes exclusive use of data from the XMM-Newton observatory. In the next Section, we outline briefly the used X-ray observations.

## 2.2 X-ray Observations

In this thesis, we investigate X-ray emission from two magnetically active Sun-like stars: AB Doradus and HR 1099. AB Doradus, a rapidly rotating member of a quadruple star

Table 2.1: Log of the observations of AB Dor and HR 1099 with XMM-Newton.

| Set | Observation ID | Instrument | Start time UTC | | Exposure (s) | Offset (′) | Src Radius (") | Bkg Radius (") | Mode | Filter |
|---|---|---|---|---|---|---|---|---|---|---|
| | | | AB Dor | | | | | | | |
| S1 | 0123720301 | PN | 27/10/2000 | 15:23:55 | 55700 | 0.145 | 70 | 50,50 | Small Window | Medium |
| | | MOS | 27/10/2000 | 15:10:06 | 56049 | 0.145 | 110 | 110 | Full Frame | Medium |
| | | RGS | 27/10/2000 | 15:01:40 | 58908 | 0.145 | | | | |
| S2 | 0134520701 | PN | 22/05/2001 | 17:05:58 | 48220 | 0.145 | 70 | 50,50 | Small Window | Medium |
| | | MOS | 22/05/2001 | 16:50:15 | 49019 | 0.145 | 80 | 80 | Full Frame | Medium |
| | | RGS | 22/05/2001 | 16:43:55 | 49607 | 0.145 | | | | |
| S3 | 0412580701 | PN | 03/01/2011 | 02:10:27 | 10000 | 0.009 | 7.5,55* | 45,32 | Small Window | Thick |
| | | MOS | 03/01/2011 | 02:07:20 | 12300 | 0.009 | 50 | 50 | Small Window | Thick |
| | | RGS | 02/01/2011 | 16:58:57 | 56051 | 0.009 | | | | |
| S4 | 0412580801 | PN | 01/01/2012 | 02:09:42 | 10001 | 0.009 | 65 | 46,46 | Small Window | Thick |
| | | MOS | 01/01/2012 | 02:06:59 | 9999 | 0.009 | 48 | 48 | Small Window | Thick |
| | | RGS | 31/12/2011 | 15:41:48 | 60770 | 0.009 | | | | |
| S5 | 0791980101 | PN | 07/10/2016 | 01:32:25 | 10019 | 0.009 | 20,68* | 45,45,25 | Small Window | Thick |
| | | MOS | 07/10/2016 | 01:26:56 | 10077 | 0.009 | 54 | 54 | Small Window | Thick |
| | | RGS | 07/10/2016 | 01:26:47 | 98313 | 0.009 | | | | |
| S6 | 0810850501 | PN | 30/09/2019 | 22:26:59 | 12000 | 0.009 | 60 | 45,40 | Small Window | Thick |
| | | MOS | 30/09/2019 | 22:18:37 | 11999 | 0.009 | 47 | 47 | Small Window | Thick |
| | | RGS | 30/09/2019 | 01:55:59 | 99485 | 0.009 | | | | |
| | | | HR 1099 | | | | | | | |
| A1 | 0116150601 | PN | 29/01/2000 | 15:41:01 | 54234 | 0.145 | 55,15* | 40,40 | Full Frame | Thick |
| A2 | 0791980501 | PN | 25/02/2020 | 12:15:40 | 10000 | 0.145 | 60 | 43,42 | Small Window | Thick |
| | | RGS | 25/02/2020 | 01:30:57 | 48917 | 0.145 | | | | |

* The selected region corresponds to the inner and outer radii of the annulus region used for pile-up removal.

system, is known for its strong magnetic activity. For this study, we utilized 6 XMM-Newton observations taken between 2000 and 2019, focusing on 13 prominent X-ray superflares out of 21 flares identified across the dataset. HR 1099, an active RS CVn-type binary system, was observed 32 times with XMM-Newton between 2000 and 2019. Upon evaluation of the Pipeline Processing System (PPS) products, only 16 observations were found to be suitable for the scientific analysis. Among these, six displayed flaring activity, with four flares previously examined in earlier research. The log of observations, which are analyzed in this thesis, is given in Table 2.1. In the next Section 2.3, we elucidate the data reduction process.

## 2.3 Data Reduction Procedure

The data reduction and analysis of the XMM-Newton observations were carried out using the Science Analysis System (SAS) software, version 18.0.0, along with the latest

calibration files. We processed the data from both the EPIC (European Photon Imaging Camera) and RGS (Reflection Grating Spectrometer) instruments to extract high-quality light curves and spectra for temporal and spectral studies of AB Dor and HR 1099. The reduction procedure and analysis strategies for each instrument are discussed separately below.

### 2.3.1 EPIC Data Reduction

The raw EPIC data from the PN and MOS detectors were processed using the SAS tasks EPPROC and EMPROC, respectively, to generate the calibrated event files. These event files contain detailed information about every detected X-ray photons during an observation, such as detector position, sky coordinates, photon arrival time, energy, etc. These tasks correct for the instrumental effects, such as gain shifts and CCD alignments, and produce cleaned datasets suitable for the scientific analysis. For all EPIC data, we restricted our analysis to the 0.3–10.0 keV energy range to avoid contamination by elevated particle background at higher energies.

To identify and exclude time intervals affected by the soft proton flaring, we used the EVSELECT task to filter events with the energies above 10 keV. Light curves generated in this range were visually inspected, and background flares were removed using appropriate time or count rate filters, ensuring the removal of high background periods while preserving the source data.

Further, we checked for the presence of pile-up in EPIC detectors. Pile-up occurs when multiple X-ray photons are detected in the same or adjacent CCD pixels within a single readout frame, leading to an inaccurate energy reconstruction and misclassification of the events. This effect was evaluated using the SAS task EPATPLOT, which diagnoses pile-up by analyzing the distribution of single, double, triple, and quadruple events in the event data. Under normal conditions, these event patterns follow predictable ratios that

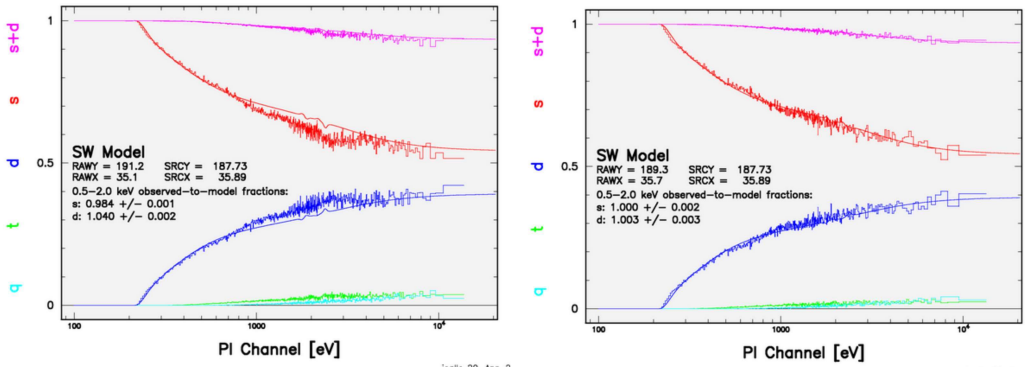


Figure 2.4: Figure showing the PN pattern distribution versus energy (PI channels) as produced by the EPATPLOT task. Panel (a) illustrates the presence of pile-up, evidenced by clear deviations of the single, double, and single+double event distributions from the expected model curves. Panel (b) displays the pattern distribution after pile-up mitigation by excluding the inner core of the source region, resulting in distributions that align closely with the model predictions.

vary with energy, but pile-up leads to the deviations, typically a reduction in the single events and an excess of doubles, due to overlapping charge deposits. The diagnostic plot from EPATPLOT helps in identifying these anomalies through a comparison of spectral and fractional distributions of event types as shown in Fig. 2.4. In cases where pile-up was significant, it was mitigated by extracting events from an annular region around the source in place of a circular region, to exclude the piled-up central core. In pile-up free data, a circular source region was chosen, while background events were selected from nearby source-free regions on the same CCD as demonstarted in Fig. 2.5.

Further, the X-ray light curves and spectra were extracted from these filtered and pile-up corrected event files. Light curves were corrected for the instrumental effects and background contributions using the EPICLCCORR task. For spectral analysis, we employed the ESPECGET task to extract source and background spectra along with associated response files: ARF (Ancillary Response File) via ARFGEN and RMF (Redistribution Matrix File) via RMFGEN. All spectra generated via above mentioned procedure were grouped to ensure a minimum of 20 counts per energy bin using the GRPPHA tool, optimizing the data for $\chi^2$ fitting in subsequent spectral modeling.

### 2.3.2 RGS Data Reduction

The RGS data reduction was performed independently for RGS1 and RGS2 using the SAS task RGSPROC, which calibrates the event lists and generates the necessary intermediate data products, including spectra and response matrices, typically in the 0.3–2.0 keV energy range. To check for the background effects in the RGS detector, one must account for the periods of elevated particle background, which can occur due to a solar activity or the Earth's radiation belts. A standard approach involves inspecting the event data from CCD 9 of the RGS, as it is closest to the optical axis of the telescope and therefore more sensitive to the background flares. Once the high-background intervals were excluded, the task RGSLCCORR was used to extract background-subtracted light curves. Finally, the RGSCOMBINE task was used to merge the calibrated spectra from RGS1 and RGS2, which

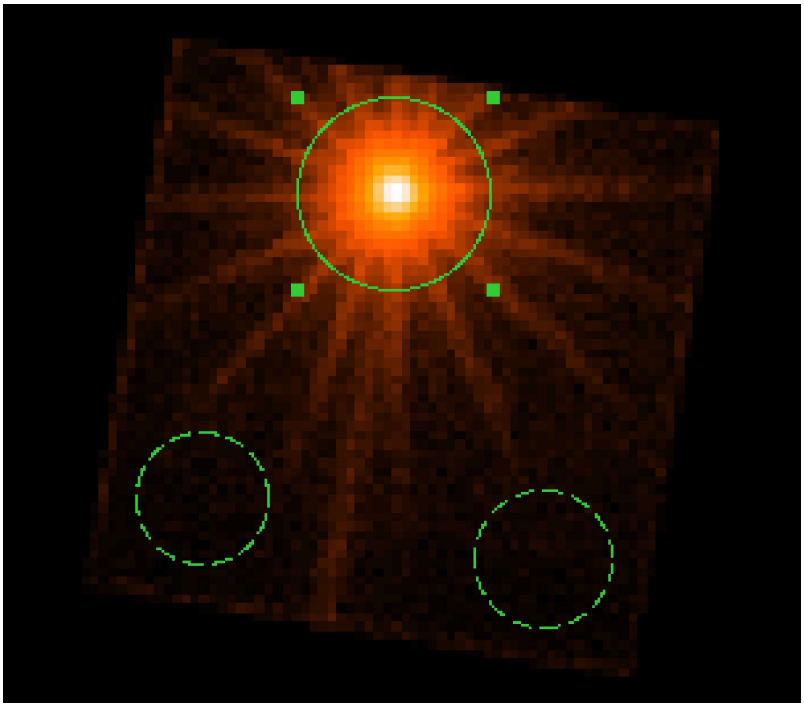

Figure 2.5: Illustration of the source and background extraction regions on the detector: The solid green circle marks the selected source region centered on the star, while the dashed green circles indicate the nearby background regions used for generating light curves and spectra.

were then grouped appropriately for the high-resolution spectral analysis. The grouped spectra contain the information about the effective area of the instrument provided by the Ancillary Response File (ARF), and the energy resolution of the detector defined by the Redistribution Matrix File (RMF). In the next Section 2.4, we describe some data analysis techniques that are used in the present thesis.

## 2.4 Analysis Techniques

After generating all the necessary products like light-curves and spectra, the X-ray spectral fitting software XSPEC (version 12.12.1) was used to fit the source spectra based on a theoretical source spectrum (Arnaud, 1996). The observed source spectrum g(E) consists of counts in specific instrument channels C(I), which are related to the true source spectrum through the instrument's response matrix R(I,E) by this equation:

$$C(I) = \int_0^\infty R(I,E)g(E)dE \tag{2.1}$$

This response matrix R(I,E) defines the probability that a photon of energy E will be detected in a particular channel I. Since directly inverting this relationship to recover the true source spectrum g(E) is mathematically unstable and does not provide unique solutions, XSPEC instead uses a forward-folding approach. A model spectrum g(E,p1,p2,...), defined by a few physical parameters, is convolved with the instrument response to produce a predicted count distribution $C_p(I)$. This predicted spectrum is then compared to the observed data using a fit statistic, typically $\chi^2$. The parameters of the model are iteratively adjusted to minimize the difference between observed and predicted counts, thereby identifying the best-fit model that most accurately represents the source.

$$\chi^2 = \Sigma \frac{(C_P(I) - C(I))^2}{\sigma(I)^2} \tag{2.2}$$

Here, $\sigma(I)$ is the uncertainty in channel I, usually estimated by $\sqrt{C(I)}$. The $\chi^2$ statistic is a standard measure of goodness-of-fit, where a reduced chi-square value ($\chi^2_\nu = \chi^2/\nu$, where $\nu$ is the degree of freedom) close to one indicates a good fit, meaning that the model is consistent with the data within the estimated uncertainties. Values significantly above suggest a poor fit, whereas values below one suggest overestimated errors. To minimize the fit statistic, XSPEC uses a modified Levenberg-Marquardt algorithm and finds the best-fit model parameters by analytically estimating second derivatives (Moré, 1978). As a local optimizer, it can get stuck in a local minimum, so sensible initial parameter values are important for reliable results.

### 2.4.1 Stellar Coronal Plasma Models

Stellar coronae emit distinct X-ray spectra that reveal valuable information about their physical conditions. To interpret these spectra, coronal plasma models are employed under several foundational assumptions. These models suggest that the plasma is primarily heated through collisional processes and cools by radiating energy. They also assume ionization equilibrium, where ionization and recombination rates are balanced, and that the plasma is optically thin, allowing radiation to escape without reabsorption. Moreover, it is presumed that both electrons and ions follow Maxwellian energy distributions, and the effects of external radiation fields on ionization are minimal. Although these assumptions simplify the complex physics of stellar coronae, they are appropriate for the conditions involving low electron density and high temperatures. Using accurate atomic data, coronal plasma models can calculate the emissivity of the plasma as a function of energy for given values of the temperature, density, and elemental abundances. One such model is the Astrophysical Plasma Emission Code (APEC). It uses atomic data from the Astrophysical Plasma Emission Database (APED) to simulate both continuum and line emissions from

hot, optically thin plasmas (Smith et al., 2001). APEC is widely used due to its ability to compute emission spectra directly based on plasma parameters.

However, it assumes uniform, solar-like abundances for all elements. For more flexibility, the VAPEC (Variable Abundance APEC) model extends APEC by allowing individual elemental abundances to be varied independently, rather than assuming solar abundances for all elements (Anders and Grevesse, 1989; Wilms et al., 2000). This is especially useful in astrophysical environments where certain elements may be enhanced or depleted relative to solar values. Together, APEC and VAPEC provide powerful tools for modeling coronal X-ray spectra and gaining insights into the physical conditions and chemical compositions of stellar coronae.